

Acoustic emission detection in concrete specimens: Experimental analysis and lattice model simulations

I Iturrioz¹, G Lacidogna² and A Carpinteri²

Abstract

In civil engineering, a quantitative evaluation of damage in materials subjected to stress or strain states is of great importance due to the critical character of these phenomena, which may suddenly give rise to catastrophic failure. From an experimental point of view, an effective damage assessment criterion is provided by the statistical analysis of the amplitude distribution of the acoustic emission signals generated by growing microcracks. A classical way to work out the amplitude of acoustic emission signals distribution is the Gutenberg-Richter law, characterized by the b -value parameter, which systematically decreases with damage growth. The damage process is also characterized by a progressive localization that can be modeled through the fractal dimension $2b = D$ of the damaged domain. In the framework of continuum damage mechanics, the progressive deterioration of the material that causes formation of macro-cracks is described by means of phenomenological damage variables usually introduced in classical constitutive relationships. Nevertheless, taking into account discrete damage mechanics, lattice models are particularly suitable to reproduce the generation of acoustic emission events, arising from the materials, during the different stages of damage growth. These models are also fundamental for the application of advanced statistical methods and non-standard mathematical methods, e.g. fractal theory. Starting from these considerations, in this work a b -value analysis was conducted in laboratory on two concrete specimens loaded up to failure. One was a prismatic specimen subjected to uniaxial compressive loading and the other was a pre-cracked beam subjected to a three-point bending test. The truss-like discrete element method was used to perform numerical simulations of the testing processes. The test results and the results of the numerical analyses, in terms of load vs. time diagram and acoustic emission data, as determined through b -value and signal frequency variations, are compared and are seen to be in good agreement.

Keywords

Concrete, lattice model, acoustic emission technique, b -value, damage parameter

¹Department of Mechanical Engineering, Federal University of Rio Grande do Sul, Porto Alegre, RS, Brazil

²Politecnico di Torino, Department of Structural, Geotechnical and Building Engineering, Torino, Italy

Corresponding author:

G Lacidogna, Politecnico di Torino, Corso Duca degli Abruzzi, 24, Torino, I0129, Italy.

Email: giuseppe.lacidogna@polito.it

Introduction

From a physical point of view, damage phenomena consist either of surface discontinuities in the form of cracks or of volume discontinuities in the form of cavities (Lemaitre et al., 1990; Krajcinovic, 1996). Macroscopically, it is difficult to tell a highly damaged volume element apart from an undamaged one since the depth of the cracks or interior defects cannot be determined. It therefore becomes necessary to identify internal variables that reflect the damage level in the material and are directly accessible to measurement (Krajcinovic, 1996; Lemaitre et al., 1990; Turcotte et al., 2003).

The most advanced method for a non-destructive quantitative evaluation of damage progression is the acoustic emission (AE) technique. Physically, AE is a phenomenon caused by a structural alteration in a solid material, in which transient elastic-waves due to a rapid release of strain energy are generated. AEs are also known as stress-wave emissions.

AE waves, whose frequencies typically range from kHz to MHz, propagate through the material towards the surface of the structural element, where they can be detected by sensors that turn the released strain energy packages into electrical signals (Carpinteri et al., 2006, 2008, 2009c; Colombo et al., 2003; Kurz et al., 2006; Lu et al., 2005; Ohtsu, 1996; Pollock, 1973; Rao and Lakshmi, 2005; Shiotani et al., 1994). In this study, USAM resonant sensors (accepting signals in the 50–800 kHz range) were used, since concrete strongly attenuates the emissions and maximum sensitivity was required to properly analyze the actual energy content. More details about this subject could be founded in Carpinteri et al. (2006, 2008, 2009c). Traditionally, in AE testing, a number of parameters are recorded from the signals, such as arrival time, velocity, amplitude, duration and frequency. From these parameters, damage conditions and localization of AE sources in the specimens are determined (Carpinteri et al., 2009a).

Using the AE technique, an effective damage assessment criterion is provided by the statistical analysis of the amplitude distribution of the AE signals generated by growing microcracks. The amplitudes of such signals are distributed according to the Gutenberg-Richter (GR) law, $N(\geq A) \propto A^{-b}$, where N is the number of AE signals with amplitude $\geq A$. The exponent b of the GR law, the so-called b -value, changes with the different stages of damage growth: while the initially dominant microcracking generates a large number of low-amplitude AE signals, the subsequent macrocracking generates fewer signals of higher amplitude. As a result, the b -value progressively reduces as the specimen approaches impending failure: this is the core of the so-called “ b -value analysis” used for damage assessment (Carpinteri et al., 2006, 2008, 2009b, 2009c; Colombo et al., 2003; Kurz et al., 2006; Ohtsu, 1996; Rao and Lakshmi, 2005; Shiotani et al., 1994).

On the other hand, the damage process is also characterized by a progressive localization that can be modeled, according to the author's prior works, through the fractal dimension D of the damaged domain. It may be proved that $2b = D$ (Aki, 1967; Carpinteri, 1994; Turcotte et al., 2003; Rundle et al., 2003; Carpinteri et al., 2008). Therefore, by determining the b -value it becomes possible to identify the energy release modalities in a structural element during the AE monitoring process. According to that approach, the extreme cases envisaged are $D = 3.0$, which corresponds to $b = 1.5$, a critical condition in which the energy release takes place through small defects evenly distributed throughout the volume, and $D = 2.0$, which corresponds to $b = 1.0$, when energy release takes place on a fracture surface. In the former case diffused damage is observed, whereas in the latter case two-dimensional (2D) cracks are formed leading to the separation of the structural element.

Moreover, in seismology, the energy released during an earthquake can be linked with seismogram amplitude, thanks to the classical expression proposed by Richter (1958), $E_s \propto A^c$, where: A is

the earthquake amplitude and $c = [1.5, 2]$ is an exponent obtained experimentally from earthquakes measurements. Another expression appearing in a seismological context, in Chakrabarti and Benguigui (1997), is $N(> = E_s) \propto E_s^{-d}$, where N is the cumulative distribution of released energy and $d = [0.8, 1.1]$ is an exponent obtained from earthquakes observations.

The similarity between AE monitoring of laboratory tests and seismic events was well explained by Scholz (1968). Scholz demonstrated that the statistical behaviour of the micro-fracturing activity observed in AE laboratory tests was similar in many respects to that observed in earthquakes, and hence the same power law applies, as long as we consider the signal trace amplitude measurements obtained by means of AE devices, rather than seismogram instrumental magnitude measures.

In this work, we used AE monitoring and numerical simulations to analyze the relationships between E_s , A and N , and to verify the fundamental relationship mentioned above.

As regards the numerical simulation, it is important to note that an alternative set of computational methods particularly suitable for the simulation of the AE, introduced during the 1960s, did not use a set of differential or integral equations to describe the model to be studied in the space domain. Different methods were invented as a function on the individual elements considered, e.g., particles or bars. The process is called by Munjiza (2009) “Computational Mechanics of Discontinua,” and it is now an integral part of cutting-edge research in different solid modelling fields. As examples of this new type of approach we can cite:

- Models obtained with a discrete particles method, originally proposed by Cundall and Hart (1989) and applied in Munjiza et al. (2004), Brara et al. (2001), Rabczuk and Belytscko (2004, 2007) and Rabczuk et al. (2007).
- Models made of bars linked at their nodes, which are known as lattice models. Among others, we should mention the works of Chiaia et al. (1997), Chakrabarti and Benguigui (1997), Krajcinovic (1996), Rinaldi and Lai (2007), Rinaldi et al. (2008) and Mastilovic (2011a, b), whose approach constitutes a very interesting way to simulate the continuum and provides qualitative information that sheds light on the fracture behaviour of quasi-brittle materials such as concrete and rocks.

The lattice model used in this work is a version particularly suitable for AE simulation originally proposed by Riera (1984) using the equivalent properties developed for a regular truss-like lattice model by Nayfeh and Hefzy (1978). Riera and other researchers extended the applications of the truss-like discrete element method (DEM) to model shells subjected to impulsive loading (Riera and Iturrioz, 1995, 1998); fracture of elastic foundations on soft sand beds (Schnaid et al., 2004); dynamic fracture (Miguel et al., 2010); earthquake generation and spread (Dalguer et al., 2001); scale effect in concrete (Rios and Riera, 2004) and rock dowels (Miguel et al., 2008 and Iturrioz et al., 2009); the determination of static and dynamic fracture mechanics parameters and crack growth simulation (Kosteski et al., 2008, 2009, 2011, 2012).

In this paper, the basic relationships between released energy (E_s), signal amplitude (A) and number of AE events (N) are presented, followed by a brief description of the lattice method (DEM). Then, the tests conducted on a prismatic concrete specimen subjected to uniaxial compressive loading (“Example 1”) and a concrete beam subjected to a three-point bending test (“Example 2”) are presented and the relative numerical models are described. Finally, the experimental results are compared with the results obtained on a lattice model.

Released energy, signal amplitude and AE events

Relationship between signal amplitude and the number of AE events

Magnitude (m) is a geophysical log-scale quantity which is often used to measure the amplitude of an electrical signal generated by an AE event. Magnitude is related to amplitude (A), expressed in volts (V), by the following equation (Shiotani et al., 1994; Colombo et al., 2003; Carpinteri et al., 2006, 2008, 2009b):

$$m = \text{Log } A \quad (1)$$

The widely accepted GR law, initially proposed for seismic events, describes the statistical distribution of AE signal amplitudes (Shiotani et al., 1994; Colombo et al., 2003; Carpinteri et al., 2006, 2008, 2009b):

$$N(\geq A) = \zeta A^{-b} \quad (2)$$

where ζ and exponent b are coefficients that characterize the behavior of the model. We shall focus our attention on coefficient b .

By rewriting equation (2) as a logarithmic equation:

$$\text{Log}(N \geq A) = \text{Log } \zeta - bm \quad (3)$$

where N is the number of AE peaks with magnitude greater than m , and coefficient b , referred to as “ b -value,” is the negative slope of the $\text{Log } N$ vs. m diagram. Microcracks release low-amplitude AEs, while macrocracks release high-amplitude AEs. This intuitive relationship is confirmed by the experimental observation that the area of crack growth is proportional to the amplitude of the relative AE signal Pollock (1973).

From equation (3), we find that a regime of microcracking generates weak AEs, and therefore leads to relatively high b -values (raising the threshold m , gives rise to a fast decline in the number of surviving signals). When macrocracks start to appear, instead, lower b -values are observed.

Therefore, the analysis of the b -value, which changes systematically with the different stages of fracture growth (Carpinteri et al., 2006, 2008, 2009b, 2009c; Colombo et al., 2003; Kurz et al., 2006; Ohtsu, 1996; Rao and Lakshmi, 2005; Shiotani et al., 1994), has been recognized as a useful tool for damage level assessment. In general terms, the fracture process moves from micro to macrocracking as the material approaches impending failure and the b -value decreases. While testing the materials undergoing brittle failure, the b -value is found to be around 1.5 in the initial stages. It then decreases with increasing stress level to ≈ 1.0 and even less as the material approaches failure (Carpinteri et al., 2006, 2008, 2009b, 2009c; Colombo et al., 2003; Rao and Lakshmi, 2005).

Furthermore, as pointed out in Carpinteri et al. (2009b), the statistical analysis of b -values is closely correlated with the fractal geometry approach in the damage and fracture mechanics of heterogeneous materials. Fractal geometry is the natural tool to characterize self-organized processes, emphasizing their universality and the scaling laws arising at the critical points.

Relationship between released energy and signal amplitude

For the purposes of this study, the dynamic energy balance is defined with reference to single crack embedded in a generic tridimensional solid. For the sake of simplicity, assuming that the material

has a linear elastic behavior up to crack propagation and ignoring gravitational energy, we can write:

$$U = (-W + E_{ele}) + E_d + E_k \quad (4)$$

where W is the work done by external forces, E_{ele} is the change in internal strain energy, E_d is the energy dissipated during the fracture process and E_k is the kinetic energy released during the process.

As observed by Scholz (2002), in dynamic conditions, the equilibrium energy balance is:

$$\dot{U} = 0 = (-\dot{W} + \dot{E}_{ele}) + \dot{E}_d + \dot{E}_k \quad (5)$$

When an AE signal – due to the opening of a small crack in a solid domain – is detected by a sensor applied to the surface of the solid body, by integrating equation (5) we can write:

$$E_s \equiv \Delta E_k = -\Delta E_{ele} - \Delta E_d \quad (6)$$

To obtain equation (6) from equation (5), we consider that some cracks occur without the external load being increased, and therefore $\Delta W = 0$. Equation (6) defines the energy released, E_s . In seismology, E_s represents the energy released from an earthquake; while in the case of laboratory test pieces and small-sized structures, E_s stands for the energy produced by mechanical waves captured by the AE sensors applied to the outer surface of the structure in question.

It is also possible to write a relationship between the energy released during a damage process, E_s , and the amplitude, A , of the AE signals. E_s and A are correlated by the following formula:

$$E_s = \gamma A^c \quad (7)$$

or, by rewriting equation (7) in logarithmic form, we get:

$$\text{Log } E_s = \text{Log } \gamma + c \text{ Log } A \quad (8)$$

where γ and c are adjustment coefficients.

Considering that the signal amplitudes observed during a fracture process in a body are proportional to the acceleration field, and hence to the state of stress, it may be assumed that $c = 2$. In this case we can write:

$$E_s = \gamma \sigma^2 \quad (9)$$

where γ is a coefficient that takes into account the elastic material property and σ is the stress in the analyzed domain.

By adjusting the parameters of equation (7) with the experimental results recorded from several earthquakes (for greater details see Richter (1958) and Aki and Richard (2002)), we obtained the following expression:

$$E_s = 11.4 A^{1.5} \quad (10)$$

or, by rewriting equation (10) in logarithmic form:

$$\text{Log } E_s = 11.4 + 1.5 \text{ Log } A \quad (11)$$

Based on equation (10), Scholz (1968) developed a scale-independent analytical model that can be applied both to laboratory tests and to seismic events. This model uses strong but plausible assumptions: (i) it works with anisotropic linear elastic material; (ii) all the cracks are considered to be penny-shape type, and, although they can be of different sizes, to be similar to each other; (iii) the mean stress applied to the domain is constant. This analytical model allows us to reach interesting conclusions about the b -value as defined above; for instance, the model predicts the tendency of the b -value to decrease as the fracturing process increases.

In Kanamori and Anderson (1975), different global parameters commonly applied in seismology are reviewed. The authors analyze the relationship between the elastic energy released in earthquakes, E_s , and signal amplitude, A , and point out that not all the energy dissipated is correlated with signal amplitude A ; they define an efficiency factor, η_e , to compute released energy E_s as a portion of the drop in potential energy (ΔE_{ele}) that occurs during AE events. For this reason, we can write ($E_s = \eta_e E_{ele}$), where η_e is a coefficient referred to as seismic efficiency coefficient in seismology.

Moreover, in Carpinteri et al. (2007), the authors indicate that mechanical wave signal magnitude, A , is directly correlated with the energy released, E_s , during the damage process.

Relationship between released energy and number of AE events

In Chakrabarti and Benguigui (1997), the relationship between number of events $N (\geq E_s)$ and released energy E_s was also written in the following form:

$$N(\geq E_s) = \alpha E_s^{-d} \quad (12)$$

or, by rewriting equation (12) in logarithmic form:

$$\text{Log } N(\geq E_s) = \text{Log } \alpha - d \text{Log}(E_s) \quad (13)$$

As mentioned in Chakrabarti and Benguigui (1997), (the expected d value in a seismology context must fall between 0.8 and 1.1. Moreover, it is easy to verify that by combining equations (2) and (13) we obtain equation (8), where $c = b/d$).

The fundamental relationships discussed in section “Released energy, signal amplitude and AE events” are in perfect agreement with the results obtained from the DEM lattice model simulation presented in this article, in which the correlations between the AE signals amplitude, A , the number of events, N , and the measurement of the energy released during the simulation, E_s , are analyzed.

The DEM

The version of the truss-like DEM proposed by Riera (1984) which is used in this paper is based on the representation of a solid by means of an arrangement of elements, which is only able to carry axial loads. The discrete elements representation of the orthotropic continuum was adopted to solve structural dynamic problems by means of explicit direct numerical integration of the equations of motion, assuming the mass to be lumped at the nodes. Each node has three degrees of freedom, corresponding to the nodal displacements in the three orthogonal coordinate directions. The equations that relate the properties of the elements to the elastic constants of an isotropic medium are

$$\eta = \frac{9\nu}{4 - 8\nu}, \quad EA_n = EL^2 \frac{(9 + 8\eta)}{2(9 + 12\eta)}, \quad A_d = \frac{2\sqrt{3}}{3} A_n \quad (14)$$

in which E and ν denote Young's modulus and Poisson's ratio, respectively, while A_n and A_d are the areas of the normal and the diagonal elements. The resulting equations of motion may be written in the well-known form:

$$\mathbf{M}\ddot{\vec{x}} + \mathbf{C}\dot{\vec{x}} + \vec{F}_r(t) - \vec{P}(t) = \vec{0} \quad (15)$$

in which \vec{x} is the vector of generalized nodal displacements, \mathbf{M} is the diagonal mass matrix, \mathbf{C} is the damping matrix, also assumed diagonal, $\vec{F}_r(t)$ is the vector of the internal forces acting on the nodal masses and $\vec{P}(t)$ is the vector of external forces. The dots denote time derivatives. If \mathbf{M} and \mathbf{C} are diagonal, equation (15) is not coupled and therefore the explicit central finite difference scheme may be used to integrate equation (15) in the time domain. Since the nodal coordinates are updated with every time step, large displacements can be accounted for in a natural and efficient manner. This article adopts a relationship between axial force and axial strain in the uniaxial elements, the bars, which is based on the bilinear law proposed by Hillerborg (1971). It should be noted that specific fracture energy, G_f , is directly proportional to the area below the bilinear elemental constitutive law. Another important feature of this approach is the assumption that G_f is a 3D random field with a Weibull probability distribution.

The local strain associated with maximum loading in each bar is called critical strain (ε_p). This value is also a random variable and its variability, which is measured using the coefficient of variation CV , is related to the G_f parameter by the following equation

$$CV(\varepsilon_p) = 0.5 CV(G_f) \quad (16)$$

The minimum value of ε_p determined in all the specimen bars is associated with the global strain for which a specimen loses linearity.

More exhaustive explanations of this version of the lattice model may be found in Kostas (2011, 2012). Applications of the DEM in studies involving non-homogeneous materials subjected to fracture, such as concrete and rock, may be found in Dalguer et al. (2003), Iturrioz et al. (2009), Miguel et al. (2008), Miguel et al. (2010) and Riera and Iturrioz (1998).

Example I: Concrete prismatic specimen subjected to uniaxial compression

Description of the testing set-up

A concrete specimen in compression was investigated through AE monitoring in a laboratory test. Six AE transducers (denoted by $S_{AE} 1$ to $S_{AE} 6$) were applied to the surface of the specimen, a prism measuring $160 \times 160 \times 500 \text{ mm}^3$ (see Figure 1) Carpinteri et al. (2009b).

The test was performed under displacement control using an electronically controlled servo-hydraulic material testing system (MTS 311,31 model) with a capacity of 1800 kN, by imposing a constant rate of displacement on the upper loading platen: the displacement rate was $d\delta/dt = 10^{-5} \text{ mm/s}$ during the first 10^4 seconds and after that it was increased to 10^{-4} mm/s up to failure.

This kind of machine is controlled by an electronic closed-loop servo-hydraulic system (Figure 2(b)). It is therefore possible to perform tests under load or displacement control. Displacement values are recorded by means of four strain gauges (HBM 1-LY41-50/120 model) placed on the specimen surface. In spite of the low value chosen for the displacement rate, the specimen failed in a brittle manner, as can be seen in the load vs. time (strain) diagram in Figure 2(a), where the linear branch is seen to extend almost throughout the entire duration of the test.

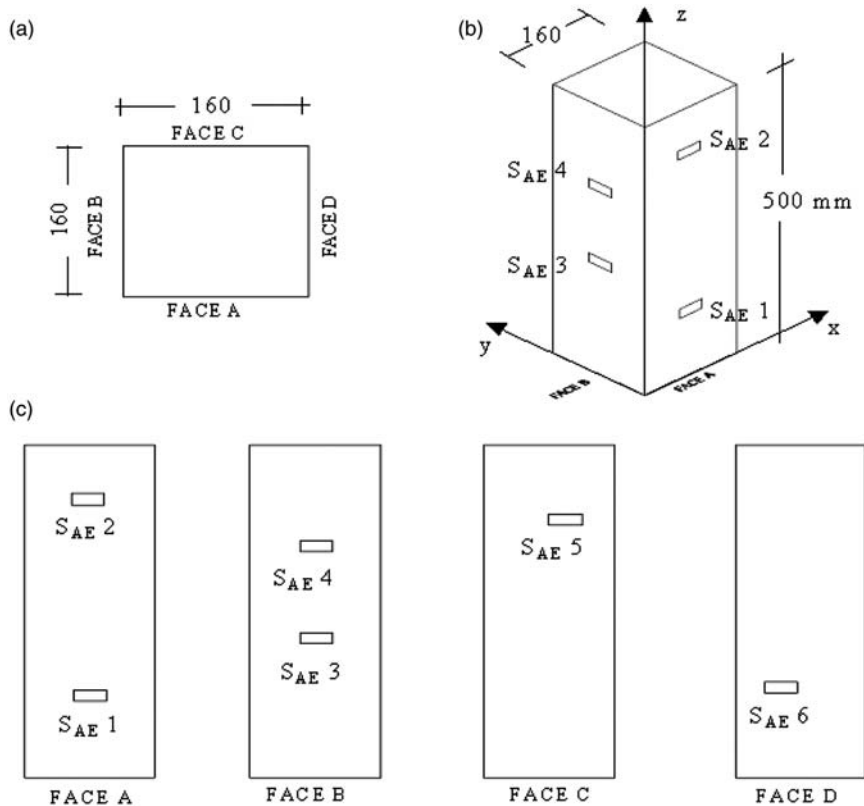


Figure 1. Concrete specimen in compression. (a) Cross-section of the specimen. (b) Axonometric projection showing the arrangement of the AE sensors. (c) Front views of the four specimen faces. AE: acoustic emission.

The characterization of the fracture process was carried out using the b -value analysis. The loading test was divided into three stages: a first stage, where linear elasticity was still valid, and two subsequent stages characterised by deviations from linear elasticity and the existence of damage. The b -value calculated at the earliest stage of the loading test, where linear elasticity was still valid, was 1.75, an index reflecting a low damage level. The b -values calculated in the two following stages of the damage region were 1.39 and 1.26, respectively, confirming the decreasing trend of the b -value as the damage grows (Figure 3). The final configuration of the specimen after testing is shown in Figure 8.

Description of the numerical model

The numerical model of the specimen was made from $27 \times 27 \times 86$ cubic modules. Each cubic module has a side length of $L = 6$ mm, and hence the model contains 13×10^4 nodes and 88×10^4 elemental bars. Using the load vs. time diagram, and the information described in section “Description of the testing set-up,” an initial elastic modulus of $E = 9$ GPa was obtained. This value of E is lower than the classical value for concrete (normally 35–40 GPa). This is due to the fact that the specimen had been subjected to a pre-damage process prior to conducting the main test.

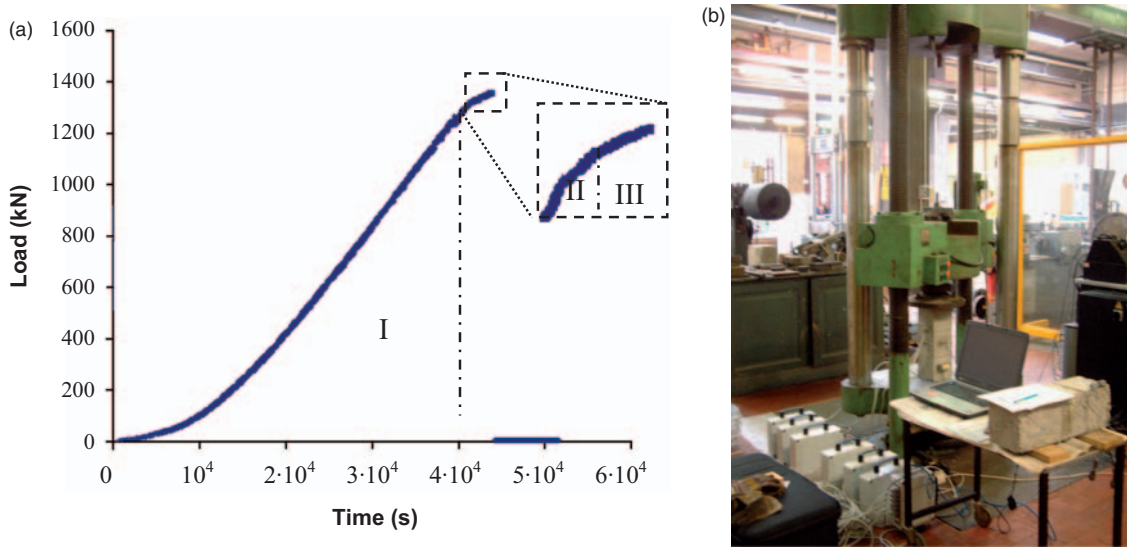


Figure 2. Concrete specimen in compression. (a) Load-time diagram of the test performed in displacement control mode. The specimen failed in a quasi-brittle manner: in region I, where linear elasticity was still valid, there is little damage (i.e., low-amplitude AE events), while in regions II and III, damage results in a deviation from linear elasticity and an increase in the AE level. (b) Photo of the MTS machine and of the specimen during the test. The devices used to detect the AE signals can be observed on the left. AE: acoustic emission.

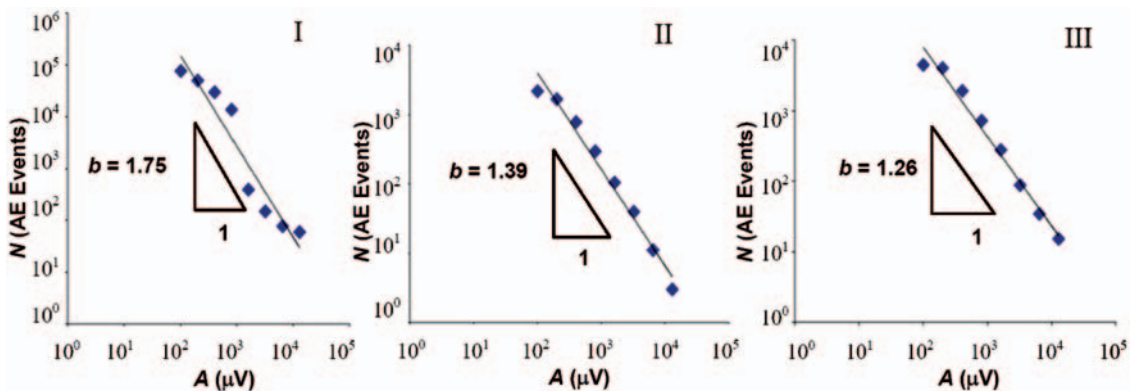


Figure 3. Concrete specimen in compression: b -values during the three stages of the loading test. It should be pointed out that event amplitudes, A , are plotted on the x -axis, in lieu of the magnitudes, m .

The specimen was subjected to uniform compressive loading up to 1300 kN for 2 consecutive days and subsequently unloaded. During the main test, the damaged specimen was reloaded up to collapse by applying the *displacement rates* given in section “*Description of the testing set-up*” and was monitored by AE sensors throughout the test. The material properties summarized in Table 1 were used in the DEM simulation.

Model configuration and applied boundary conditions are shown in Figure 8(d). Parameter G_f is defined as a random field with the mean value and the variation coefficient given in Table 1, using a probability Weibull density distribution, and a correlation length equal to the level of discretization ($L = 6$ mm).

A virtual sensor was placed in the position shown in Figure 1 (S_{AE} 1). The acceleration perpendicular to the sensor surface was captured by the same virtual sensor and interpreted as a measure of the AE signals.

Example 2: Three-point bending test

Description of the testing set-up

In this example, a specimen was subjected to a three-point bending test and the AEs generated by growing microcracks were monitored. The specimen was a prism measuring $8 \times 15 \times 70$ cm, with a central 5-cm notch cut into it beforehand to produce a central crack, and with a fiber content of 40 kg/m^3 resulting in a Young's modulus of 35 GPa. The test was performed under displacement control by imposing a constant displacement rate of 10^3 mm/s.

Five AE transducers were secured to the specimen at the points shown in Figure 4(a). The load vs. time curve obtained for the specimen, with its softening branch characterizing the AE activity, is shown in Figure 5(a).

In order to investigate the behavior of the specimen by means of the b -value analysis, the load vs. time diagram was broken down into three stages: a first stage $[t_0, t_1]$ extending from the initial time to peak load, a second stage $[t_1, t_2]$ going from peak load to the peak of AE activity, or mainshock, and a third stage $[t_2, t_p]$ going from the mainshock to the end of the process.

The b -values are shown for each stage in Figure 5(b): the values exhibited a decreasing trend, ranging from 1.49 to 1.11, as the specimen approached failure. The minimum value was obtained in the softening branch of the load vs. time curve, and it became very close to the lower limit of 1 theoretically predicted by Carpinteri et al. (1994, 2006, 2008, 2009c), as confirmed by the b -values observed in most of specimens tested up to the failure.

Description of the numerical model

The numerical model was made from $140 \times 16 \times 30$ cubic modules. Each cubic module has a side length of $L = 5$ mm, and therefore the model contains 14×10^4 nodes and 95×10^4 elemental bars. Using the load vs. time diagram shown in the Figure 5(a), and the information given in section "Description of the testing set-up," we obtained $E = 35$ GPa. The other parameters adopted are summarized in Table 2.

Boundary conditions are shown in Figure 4(a). The excitation was applied to the model by introducing a predetermined displacement at a velocity that did not give rise to significant inertial effects in the model. The pre-crack was simulated so as to attenuate the strength of the bar in the pre-cracked zone.

Numerical results and comparison with the test results

Below are the numerical results obtained from the lattice model calculations and their comparison with the experimental values. The results obtained for the two cases described above are shown side by side, whenever feasible, to facilitate their evaluation.

Table 1. Main mechanical properties used in the DEM simulation.

E (Elastic Young Modulus) = 9 GPa
ρ (Density) = 2500 kg/m ³
$\mu(G_f)$ = 560 N/m (Mean value), $CV(G_f)$ = 50%
$\mu \varepsilon_p$ (Mean critical strain) = 2.4×10^{-4}
DEM: discrete element method.

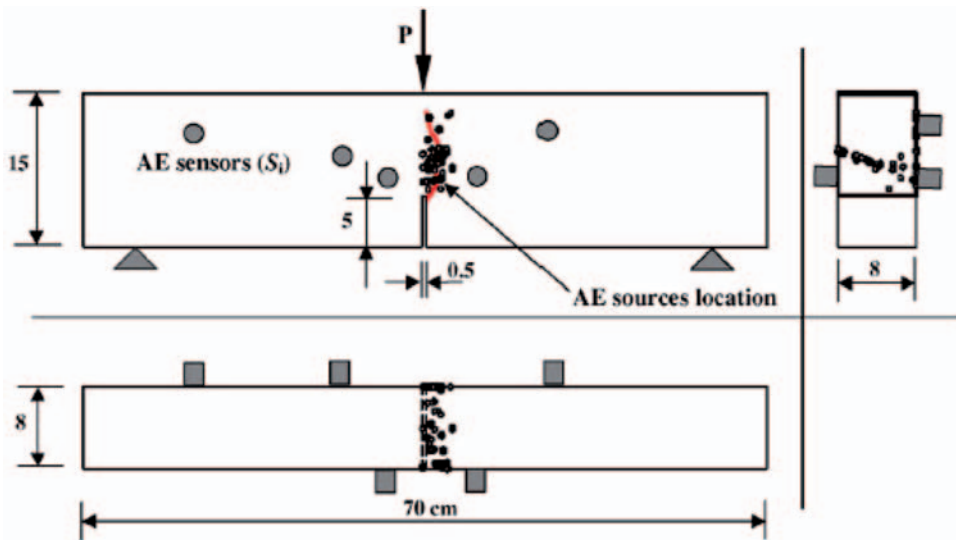


Figure 4. Three-point bending test. Geometric configuration, AE sensors position and the boundary conditions used in the test.

AE: acoustic emission.

Load vs. time, and energy balance

The load vs. time diagrams obtained experimentally and from the numerical simulations are compared in Figure 6. The peak loads and the areas of the curves plotted for both tests (the uniaxial test and the three bending point test) turned out to be similar.

For the compression test, the loss of linearity near the peak load, reflected in the experimental curve, shows that maximum damage occurred in the final part of the diagram and a sharp drop in stress can also be clearly seen in the simulation curve during the second part of the process. The shape of the experimental and theoretical curves obtained for the three-point bending test is similar too.

However, if we compare the curves plotted for the experimental results obtained in both tests, we notice that overall behavior is totally different: the compression test is characterized by catastrophic collapse, whilst in the three-point bending test a ductile response is observed after the peak load has been reached.

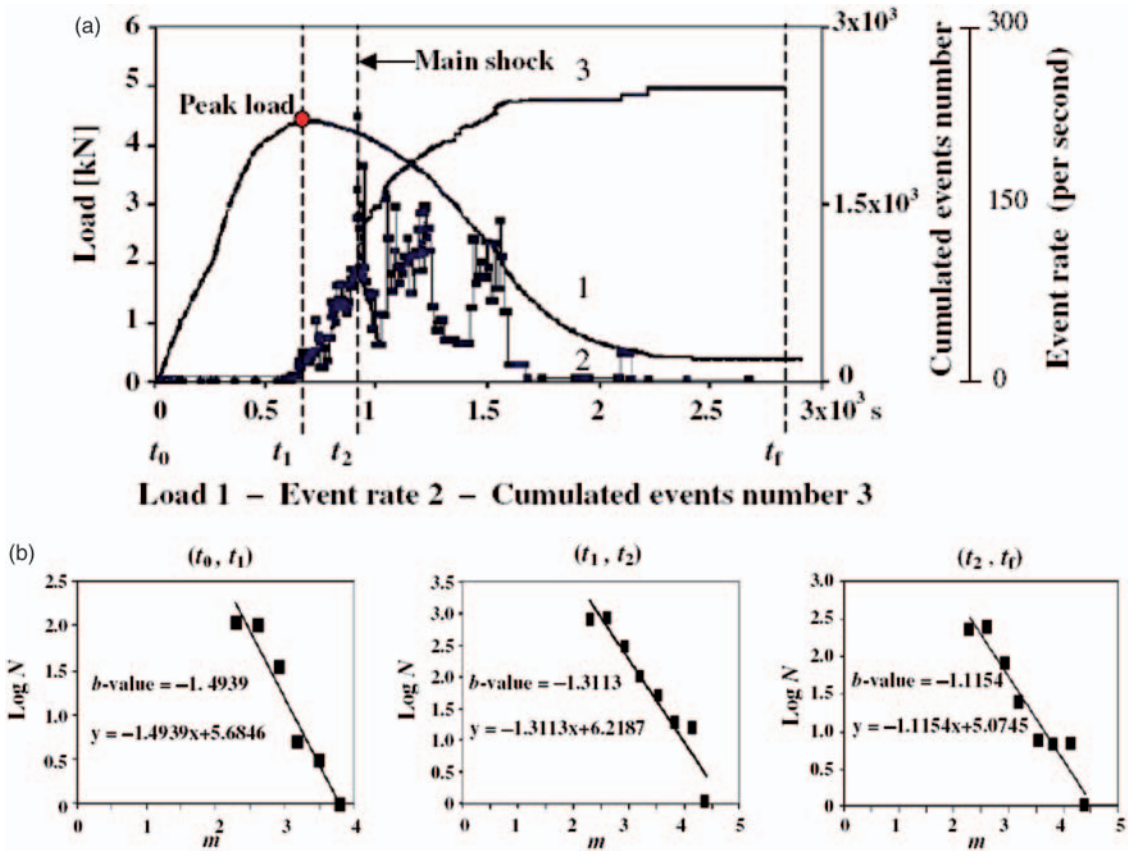


Figure 5. Three-point bending test. (a) Load vs. time curve and AE activity. (b) b -values during the loading test. AE: acoustic emission.

Figure 7 shows the results in terms of energy balance. The energy values were normalized to facilitate the comparison between the two cases. In the case of the compression test, the energy balance gives a great quantity of elastic energy (95% of the external work applied) at final collapse, for this reason a catastrophic failure is expected. In the case of the three-point bending test, the external work applied over the beam is gradually dissipated over time, for this reason at the end of the process the available potential energy is too low to produce a catastrophic collapse.

In both examples, we notice that kinetic energy during the simulation was very low. We used, for numerical reasons, a simulated loading rate faster than the rate used in the experimental test. Moreover, in both examples it was ascertained that the rates used in the numerical models did not produce significant inertial effects. Only in the uniaxial compression test the kinetic energy increased abruptly at collapse, reflecting the catastrophic nature of the phenomenon.

Final configuration

Example 1: Concrete prismatic specimen subjected to uniaxial compression. The experimental and numerical specimen configuration pertaining to the end of the test is shown in Figure 8(a)

Table 2. Main mechanical properties adopted in the DEM simulation.

E (Elastic Young Modulus) = 35 GPa
ρ (Density) = 2500 kg/m ³
μ (G_f) = 130 N/m (Mean value), CV(G_f) = 25%
μ (ε_p) (Mean critical strain) = 6.4×10^{-5}

DEM: discrete element method.

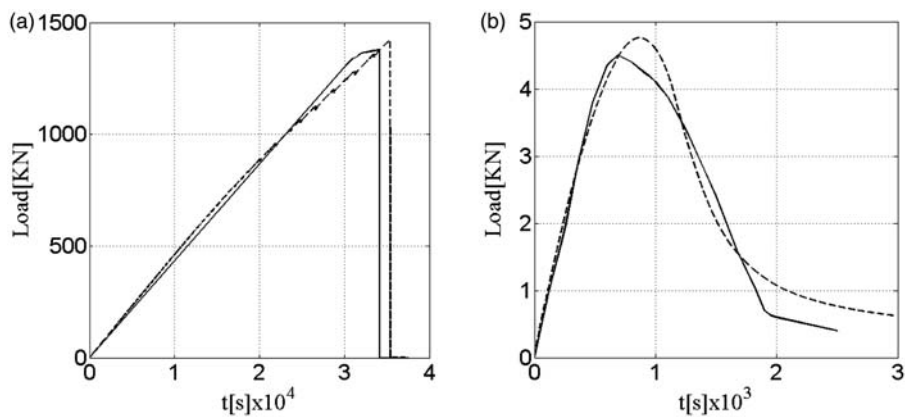


Figure 6. Load vs. time, comparison between experimental results (continuous line) and numerical simulation values (dashed line). (a) Uniaxial compression test. (b) Three-point bending test.

and (b), respectively. In these charts it is possible to appreciate that the upper sections of the specimen are the most damaged and that cone-shaped ruptures have occurred near the specimen ends. This is due to the confinement of transverse displacements at both ends (see Figure 8(d)).

In a configuration close to collapse, the transverse strain map shows (light grey portions in Figure 8(c)) the most badly damaged regions of the specimen subjected to high strains. From this figure it is also possible to understand how the main fracture mechanism occurs when ultimate strength is reached with the transverse bars (perpendicular to the direction of loading) subjected to tension.

Example 2: Three-point bending test. Two photographs of the beam in its final configuration and a detail of the DEM final configuration are given in Figure 9. In the DEM model, the fractured bars are denoted in dark grey, while light grey denotes bars only partially damaged. Undamaged bars have been omitted to improve the visualization.

In Figure 9(d) and (e), two lateral views of the damage configuration are shown, one at $t = 1200$ s (close to the peak load) and the other at $t = 2800$ s (close to the final collapse). The general configurations obtained from the numerical and experimental results are similar.

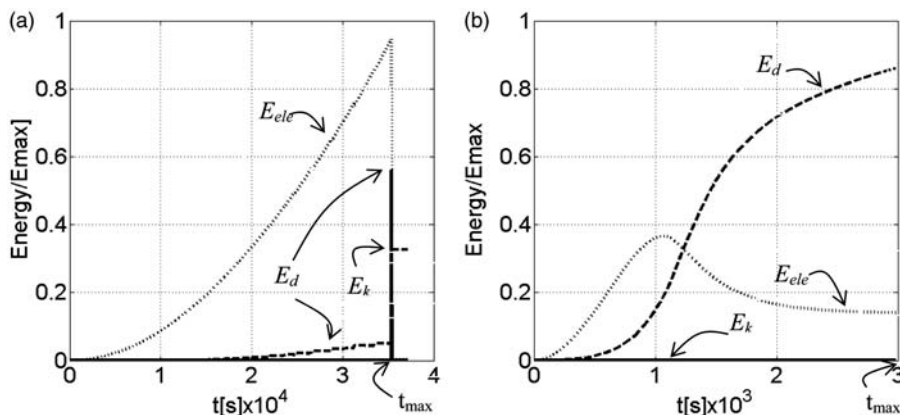


Figure 7. Normalized energy balance vs. time (E_{ele} : elastic energy, E_k : kinetic energy, E_d : dissipated energy; $E_{max} = E_{ele} + E_k + E_d$ at t_{max}). (a) Uniaxial compression test ($E_{max} = 4888$ Nm). (b) Three-point bending test ($E_{max} = 0.65$ Nm).

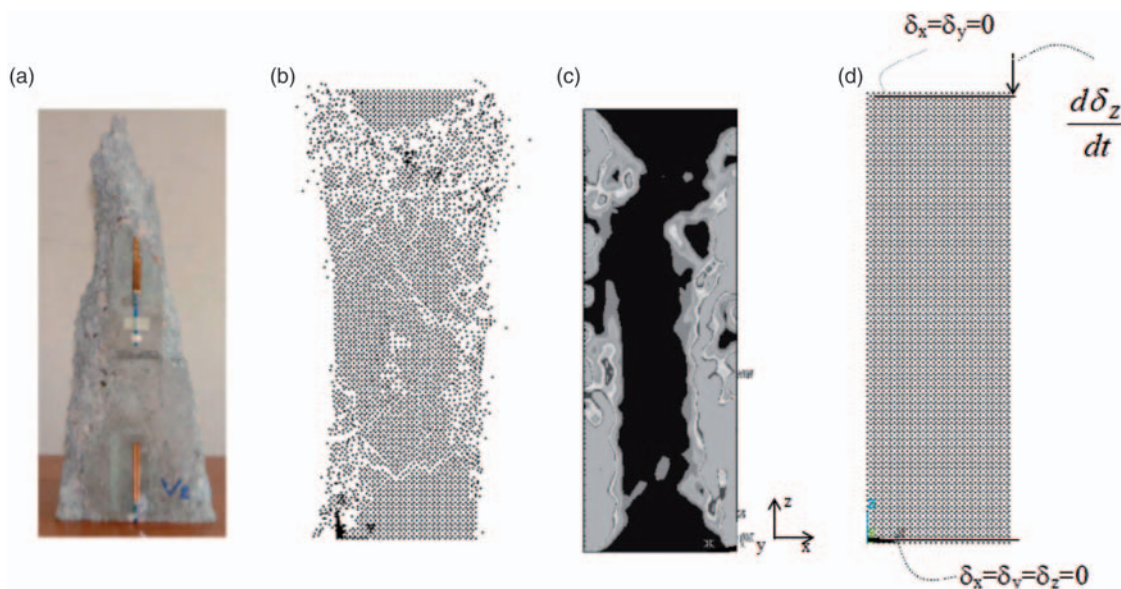


Figure 8. (a) Experimental rupture configuration. (b) Numerical rupture configuration, plotting of the nodes. (c) Map of damage (severe damage is denoted in light grey). (d) Initial configuration in which the applied boundary conditions are shown.

In Figure 10(a) and (b), the transverse sections of the beam in $x = L/2$, at $t = 1200$ s and $t = 2800$ s, show the bars damaged and fractured during the loading process. In Figure 10(c), we see a detail of the lateral view close to the central crack. The information shown in these pictures could be used to compute the fractal dimension of the fractured area, and this issue will be addressed in a future work.

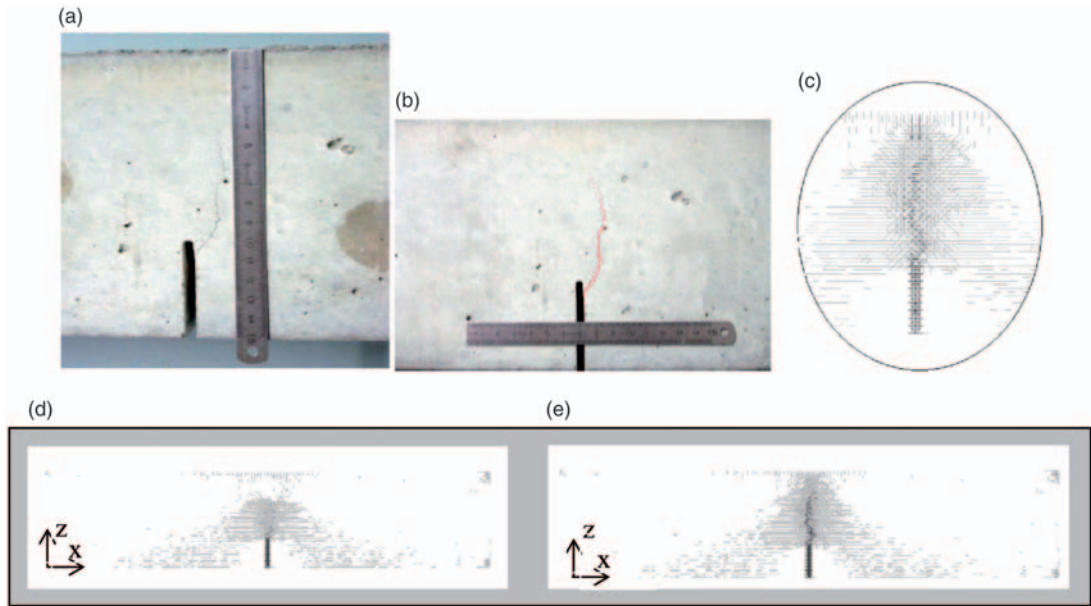


Figure 9. (a) and (b) Details of the final experimental configuration. (c) Detail of the final numerical configuration. (d) Lateral view of the damage configuration at $t = 1200$ s. (e) Lateral view of the damage configuration at $t = 2800$ s. In the numerical configuration obtained by DEM simulations, the bars that have exhausted their strength are shown in dark grey, while light grey denotes the bars only partially damaged. Undamaged bars are omitted to improve the visualization. DEM: discrete element method.

AE and N vs. time, b-value analysis

The AE event amplitudes vs. time charts obtained by DEM simulations are shown for both examples (Figure 11(a) and (b)). In these figures, the coordinate scales are normalized to facilitate the comparison between the two examples. The load variation obtained in the numerical simulation is plotted in light grey.

In Figure 12(a) and (b), the results are shown in terms of cumulated number of AE events, N , and AE event rate, N_{inst} , vs. time. In this figure too, the load vs. time curve is shown in light grey.

Finally, in Figure 13(a) and (b), the curves that link the cumulated number of AE event and their magnitudes are presented in logarithm scale. By using these curves it is possible to compute the b -value for each selected time-period.

To represent these diagrams, relative signal amplitudes were computed (we defined $A = h/h_o$, where $h_o = 100 \text{ mm/s}^2$). Then, only signals of amplitudes greater than the predetermined threshold were taken into account. We set a fixed threshold $A_{\text{thres}} = h/h_o = 30,000$ for the first example and $A_{\text{thres}} = h/h_o = 1500$ for the second. For this reason, the number of events analyzed in the simulations was limited (fewer than 200 in each example).

In general, to carry out a consistent analysis from a statistical point of view we need as a minimum a thousand events per example. By applying a lower imposed displacement rate and considering a lower value for the fixed threshold, A_{thres} , it would be possible to identify more AE peaks. However, in order to increase the number of events by considering $A > A_{\text{thres}}$, it would be necessary to increase the discretization level. For this reason, the simulations performed should be regarded as preliminary, nevertheless they are useful to capture the general trends.

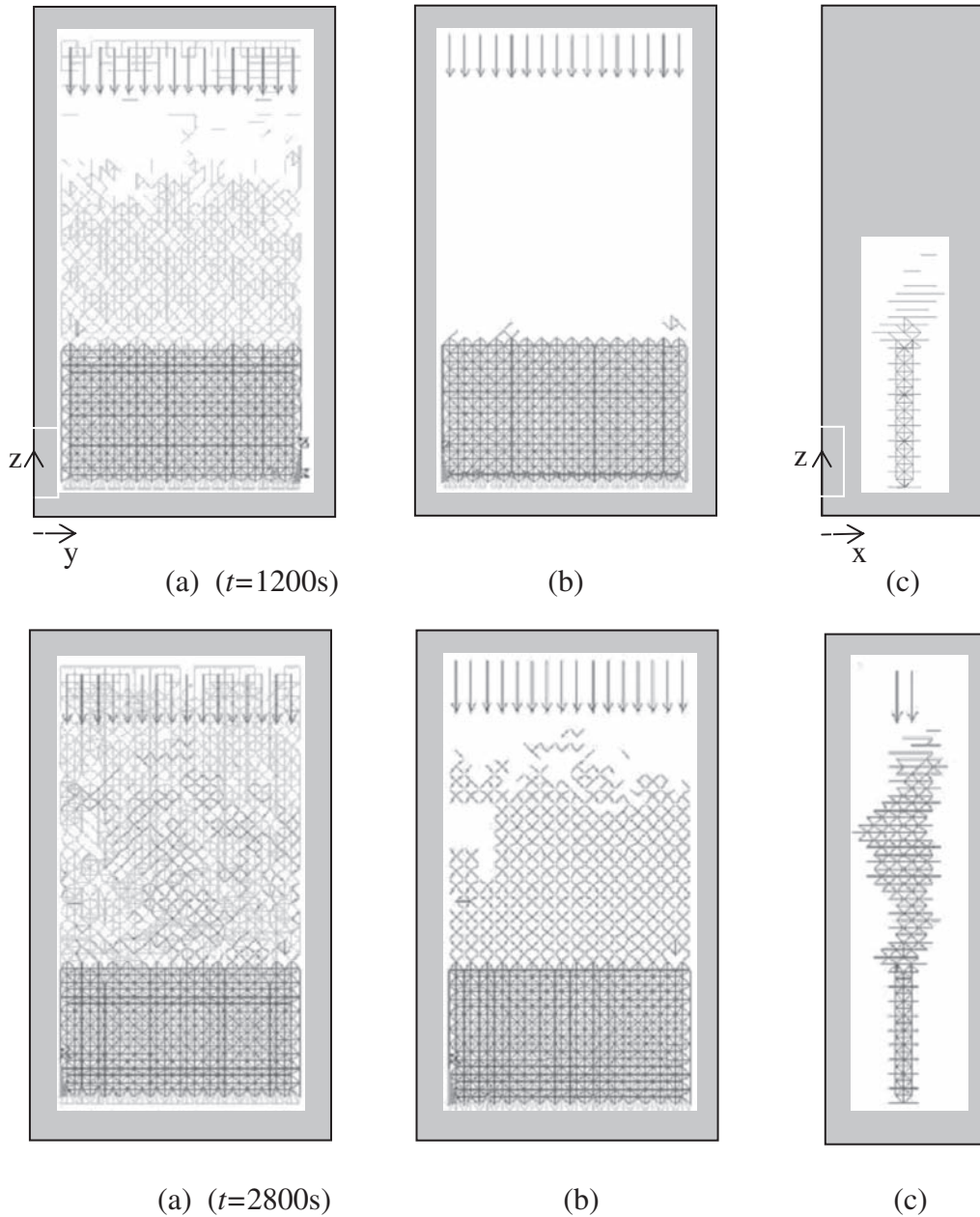


Figure 10. (a) Central crack for $x = L/2$, only the fractured and damaged bars are shown. (b) Central crack for $x = L/2$, only the fractured bars are shown. (c) Detail of the side view of the beam with only the fractured bars shown. The three figures at the top were plotted at $t = 1200$ s, the three figures below were plotted at $t = 2800$ s. The bars that have exhausted their strength are denoted in dark grey, while light grey indicates bars only partially damaged. Undamaged bars have been omitted to improve the visualization.

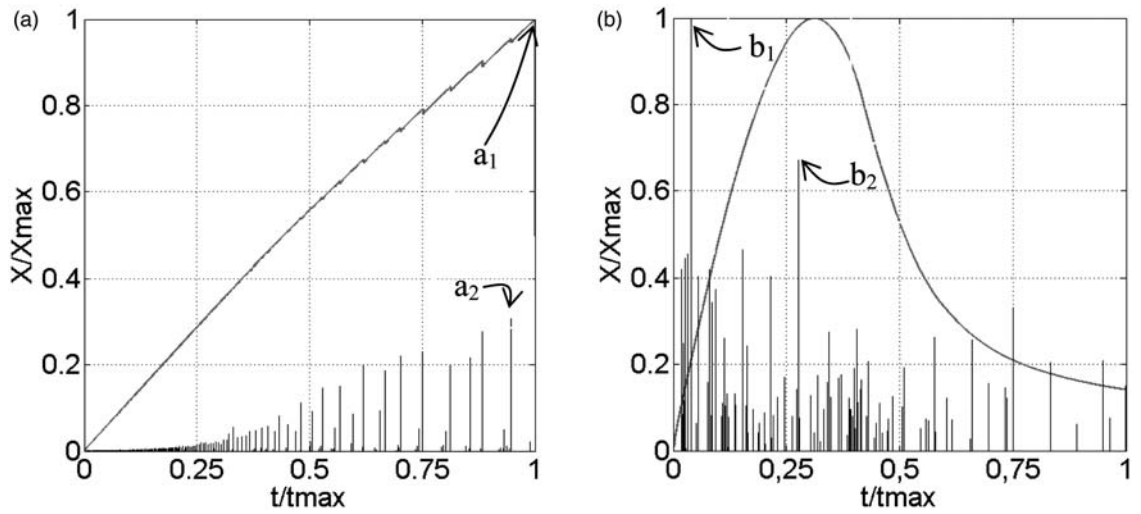


Figure 11. Load vs. time (continuous line) and AE events amplitude vs. time (vertical bars). Both coordinate axes were normalized to the maximum value. (a) Uniaxial test. (b) Three-point bending test.

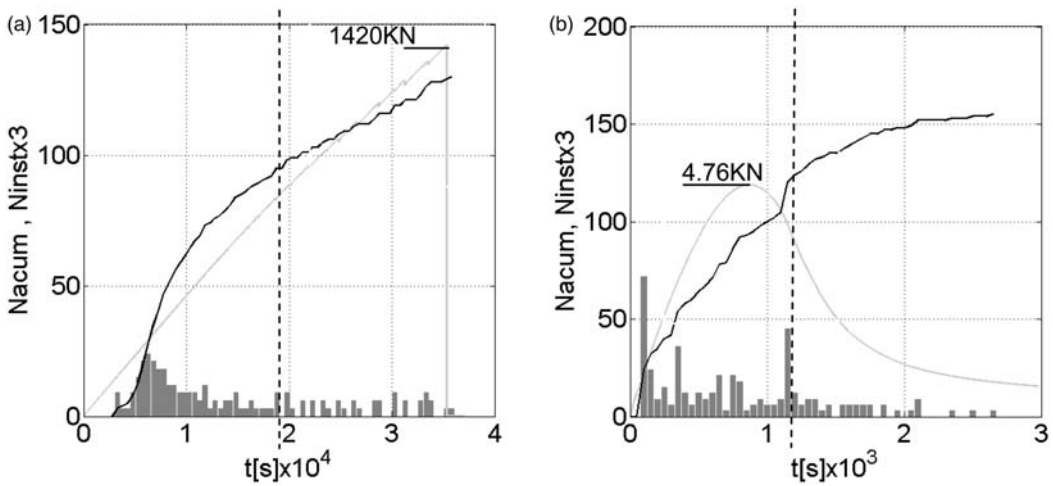


Figure 12. Cumulated number of AE events, N , AE events rate, N_{inst} , and load vs. time diagrams. (a) Uniaxial test. (b) Three-point bending test.
 AE: acoustic emission.

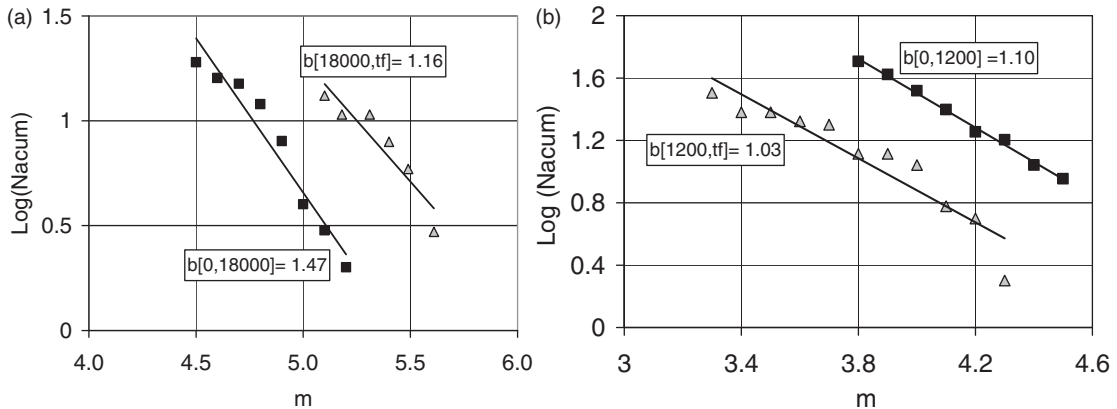


Figure 13. b -values obtained from the numerical simulation of the damage process. (a) Uniaxial test. (b) Three-point bending test.

By comparing the two examples we find that:

- (i) AE event amplitudes in the uniaxial compression test are shown in Figure 11(a). Event amplitude is seen to increase smoothly throughout the loading process up to the catastrophic collapse, which is characterized by the highest amplitude AE event, labeled (a_1) in this figure. The amplitude of this last AE event is four times as high as the amplitude of the AE peak event that occurs immediately before specimen collapse, and is labeled (a_2) in the figure.
- (ii) AE event amplitudes in the three-point bending test are shown in Figure 11(b). In this case, mechanical behavior is completely different than in the first test: here a high-amplitude event (labeled (b_1) in the figure) occurs at the beginning of the process. This AE peak event occurs due to a premature advance of the existing macro-crack. A second high-amplitude event, labeled (b_2), appears in the proximity of the maximum load. After this characteristic event, the other events are of lesser amplitude and maintain the same level until the end of the test.
- (iii) The clearly different behavior observed in the uniaxial test for cumulated AE events, N , and AE rate, N_{inst} , makes it possible to define two time intervals for the analysis of the b -value: $[0, 18000]$ s and $[18000, t_f]$ s, where t_f is the time of the final collapse. The dashed vertical line in Figure 12(a) indicates the point of separation between these two intervals.
- (iv) The cumulated AE events, N , and AE rate, N_{inst} , curves obtained from the three-point bending test are shown in Figure 12(b). In this case, two time intervals for the b -value analysis are also defined: $[0, 1200]$ s and $[1200, t_f]$ s. The dashed vertical line in Figure 12(b) indicates the point of separation between these two intervals.
- (v) By comparing Figure 12(b) with Figure 5(a), showing the experimental results, we notice that in the latter AE events do not occur until peak load, then a concentration of events emerges in the post-peak region; finally the number of AE events abruptly decreases. This last behavior is evidenced in the numerical simulation.

However, the main differences between experimental and numerical results are concentrated at the beginning of the two diagrams, where, in the experimental case, very few events are detected until the peak load is reached and, in the numerical simulation, great AE activity is observed. This discrepancy could be justified by the mechanical properties adopted in the DEM simulation, i.e. the same distribution for all the elements (see Table 2); in this manner, the stress concentration at the

tip of the pre-existing crack shows, as it should, an intense AE activity at the beginning of the loading process, while in the real specimen the local mechanical properties may be lower in the vicinity of the pre-existing crack (damaged region near the crack tip produced during specimen manufacture) than in the rest of the specimen. This event, especially at the beginning of the loading process, may have given rise to a lower AE activity.

- (vi) The b -values obtained in the two time intervals defined for the compression test are shown in Figure 13(a). The b -values obtained in the numerical simulation show a decreasing trend during the evolution of the damage process and are compatible with the experimental values. Moreover, the numerical b -values fall between the limits [1.5,1] indicated by Carpinteri et al. (2009a). In this case, we have $b = 1.47$ for the first interval and $b = 1.16$ for the second, this means that the damage process is characterized by a progressive localization identified through the fractal dimension $2b = D$ of the damage domain.
- (vii) The b -values obtained in the two time intervals defined for the three-bending point test are shown in Figure 13(b). In this case, the b -values are close to 1.0 from the start of the process. This means that the propagating crack is close to a preferential surface throughout the test duration.

AE events and energy parameters

The relationship between the energy released during the fracture process, E_s , and signal amplitude, A , is analyzed. Considering Chakrabarti and Benguigui (1997), E_s is linked with the drops in potential energy taking place during the damage process. With the aim of capturing the energy released, E_s , in the DEM context, we propose to compute the increments in kinetic energy between two successive integration times, using the following expression:

$$\Delta E_k(t_i) = E_k(t_i) - E_k(t_{i-1}) \quad (17)$$

where E_k is the kinetic energy in the discretized time during the simulation.

Using the equation (6) and the discussion carried out by Scholz (2002), briefly commented in the section “*Relationship between released energy and signal amplitude*,” we can assume the validity of the following relationship:

$$\frac{\Delta E_k(t_{Fa})}{\Delta E_k(t_{Fb})} = \frac{E_s(t_{Fa})}{E_s(t_{Fb})} \quad (18)$$

where t_{Fa} and t_{Fb} are the times at which the potential energy drops during the simulation.

In this way, equation (8) can be written in terms of ΔE_k :

$$\text{Log}(\Delta E_k(t_F)) = \text{Log} \lambda + c_{Ek} \text{Log} A(t_F) \quad (19)$$

where λ is a coefficient, and c_{Ek} is an estimate of the c coefficient in the Richter law presented in equations (7) and (8).

In a similar way, we propose rewriting equation (13), which links the number of events $N (\geq E_s)$ to released energy E_s . Using increments ΔE_k we can write:

$$\text{Log}N(> \Delta E_k(t_F)) = \text{Log} \tau + d_{Ek} \text{Log} \Delta E_k(t_F) \quad (20)$$

where τ is a coefficient and d_{Ek} is an estimate of the d coefficient in equation (13).

The variations taking place during the damage process in elastic (or potential) kinetic energy and dissipated energy are illustrated in Figure 7(a) and (b).

It is also possible to compute the increments in dissipated energy between two successive integration times using the following expression:

$$\Delta E_d(t_i) = E_d(t_i) - E_d(t_{i-1}) \quad (21)$$

In Figure 14(a), the increments in dissipated energy, ΔE_d , are plotted, and Figure 14(b) shows the variations in ΔE_k determined from equation (17). In these figures, time t_F is the time when the drop in potential energy typically occurred during the simulation process.

A typical AE event is superposed with the ΔE_d and ΔE_k increments during the simulation process in Figure 15(a). A zoom of the beginning of this AE event is shown in Figure 15(b), where it can be clearly seen that the AE signal undergoes a certain delay in time with respect to the ΔE_k and ΔE_d increments. This is due to the fact that when a localized fracture occurs in the specimen, the energy values are immediately computed, while the mechanical waves, which spread due to localized fracture in the specimen, need some additional time to reach the AE sensor.

Notice that when a drop in potential energy occurs, part of this potential energy is dissipated and part becomes kinetic energy. In Figure 16, the increments in elastic, dissipated and kinetic energy in the vicinity of a typical AE event illustrate the complex interaction between these quantities.

Finally, Figure 17(a) and (b) show the cumulative distributions in equation (20) represented in a bi-logarithmic scale. For both examples, the same intervals used in the b -values computation were used. The b , c and d coefficients computed by means of the numerical simulation are summarized in Table 3.

From Table 3 we can see that:

- (i) The $c = b/d$ ratios are close to the theoretical value 1.5 indicated by Richter (1958) as described in section “Released energy, signal amplitude and AE events.”

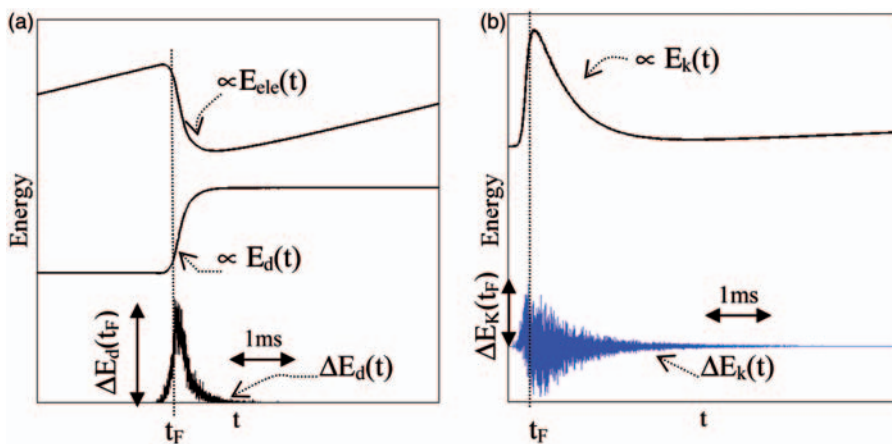


Figure 14. (a) Variations of dissipated energy increments E_d , dissipated energy E_d and elastic energy E_{ele} during the entire simulation process. (b) Variations of kinetic energy increment E_k and kinetic energy E_k during the entire simulation process.

- (ii) From the evaluation of released energy, it is possible to say that coefficients d are also sensitive to the evolution of damage, and hence d -values decrease with increasing damage and crack localization.
- (iii) From the Table it is also evident that coefficient c increases with damage, but its value does not exceed the limit of 2.

Relationship between E_s , N and A and time

Below, we extend the idea expressed in Carpinteri et al. (2007) where AE results are expressed in terms of an accumulated parameter (N , A or a measure of E_s) normalized to its maximum value vs.

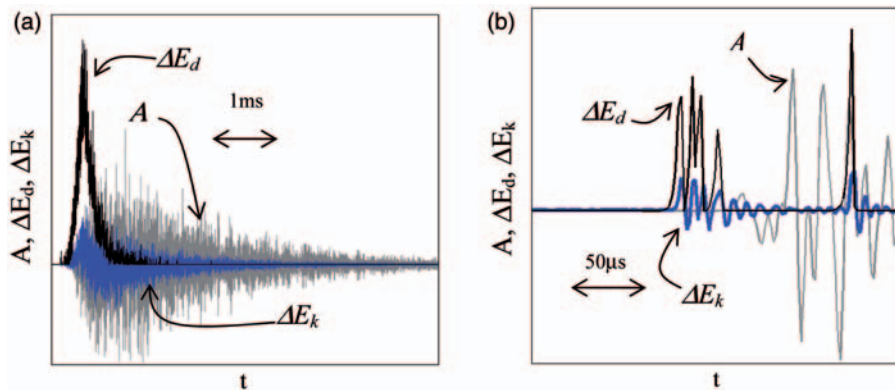


Figure 15. (a) The three types of signals overlapped. Signal amplitudes were modified to be able to put them in the same scheme. (b) Details of the beginning of the peak event. Increment in dissipated energy $E_d(t)$, increment in kinetic energy $E_k(t)$ and the AE signal produced. AE: acoustic emission.

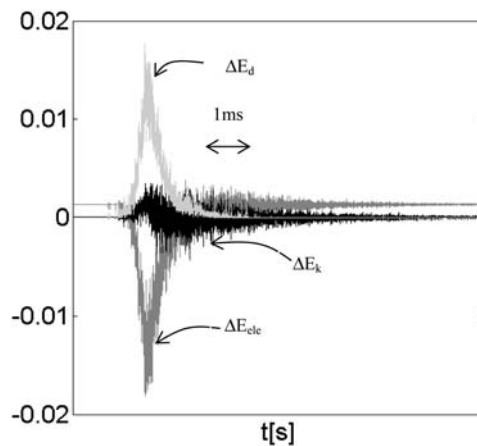


Figure 16. Increments in elastic energy (dark grey line), kinetic energy (black line) and dissipated energy (light grey line) vs. time in the vicinity of a typical AE event. The units on the vertical axis are arbitrary. AE: acoustic emission.

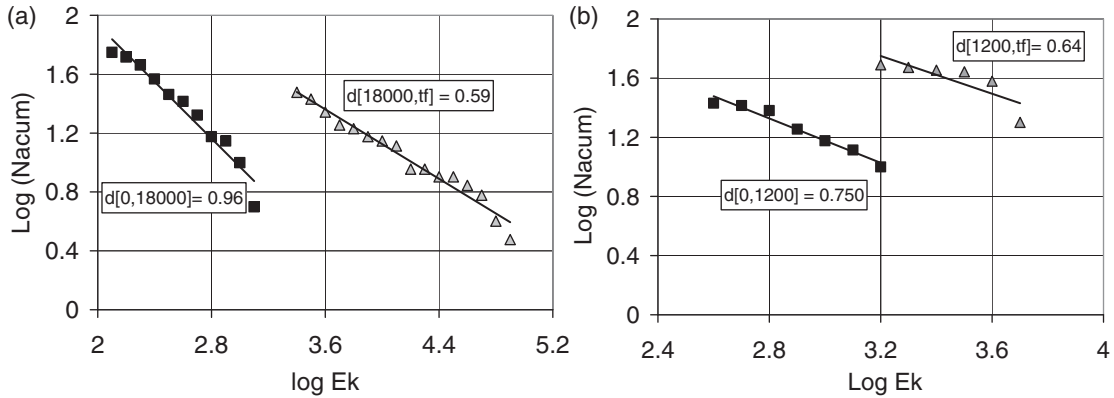


Figure 17. The *d* coefficients obtained in (a) uniaxial test and (b) three-point bending test.

Table 3. *b*, *d* and *c = b/d* coefficients for the two specimens analyzed.

Compression test		Bending test	
[0,18000]s	[18000, <i>t_f]</i> s	[0,1200]s	[1200, <i>t_f]</i> s
<i>b</i> = 1.47	<i>b</i> = 1.16	<i>b</i> = 1.1	<i>b</i> = 1.01
<i>d</i> = 0.96	<i>d</i> = 0.59	<i>d</i> = 0.75	<i>d</i> = 0.64
<i>c</i> = 1.53	<i>c</i> = 1.97	<i>c</i> = 1.47	<i>c</i> = 1.58

(*t/t_{max}*). The behaviors of these functions give us useful information about the specimen damage time-scaling.

We propose here the following relations:

$$\frac{N_{acum}}{(N_{acum})_{max}} \propto \left(\frac{t}{t_{max}}\right)^{\beta_N} \tag{22}$$

$$\frac{A_{acum}}{(A_{acum})_{max}} \propto \left(\frac{t}{t_{max}}\right)^{\beta_A} \tag{23}$$

$$\frac{\Delta E_{k_acum}}{(\Delta E_{k_acum})_{max}} \propto \left(\frac{t}{t_{max}}\right)^{\beta_K} \tag{24}$$

In the previous equations, $N_{acum}/(N_{acum})_{max}$ is the number of cumulated AE events normalized to their maximum value; $A_{acum}/(A_{acum})_{max}$ the normalized number of cumulated AE signals amplitudes and $\Delta E_{k_acum}/(\Delta E_{k_acum})_{max}$ the normalized number of cumulated kinetic energy increments related to the AE events. All the expressions are related to normalized time *t/t_{max}*.

These relationships are illustrated in bi-logarithmic scale in Figures 18(a) and 19(b) for the uniaxial compression test and the three-points bending test, respectively. In this way, the values of coefficients β_N , β_A and β_K are obtained. The same relationships are plotted on a linear scale in

Figures 18(b) and 19(b). Finally, the values of the β coefficients computed for both tests are summarized in Table 4.

It should be noted that only values greater than $t/t_{max} = 0.4$ were used to perform the regression in the bi-logarithmic diagrams. In Carpinteri et al. (2007) this point was discussed. The authors justified using only this part of the process because in the first part, $t/t_{max} \in [0, 0.4]$, the results could be highly influenced by the specific boundary conditions of the tests.

By analyzing the results presented in Figures 18, 19 and in Table 4, we find that the β coefficients give us useful information about the last part of the damage process.

Specifically, we observe that:

- (i) $\beta_N = 0.98$ indicates that in the compression test the AE events number grows at a constant rate throughout the loading process. The same information appears in the linear branch of the N_{acum} vs. time curve, shown in Figure 18(b). On the other hand, AE events amplitudes increase by a factor of $\beta_A = 2.02$, while the cumulated number of kinetic energy increments, corresponding to each AE event, increases by a higher factor: $\beta_K = 3.2$.
- (ii) Coefficients β_N and β_A have virtually the same values in the three-points bending test. The values of these coefficients indicate that not only the AE events number but also event amplitudes have a tendency to diminish as the damage process advances. The relationship between the kinetic energy and the damage process is characterized by the coefficient $\beta_K = 1.36$, which implies a smoother increase than in the compression test example.
- (iii) If we compare the β coefficients of the two examples, we find that the larger values recorded for the compression test characterize a catastrophic collapse. This information is not included in the b -values analysis that measures the damage localization process throughout the tests duration.

AE event frequency variations during the damage process

In this section, the simulation results are analyzed in terms of AE signal frequency variations. In Schiavi et al. (2011), in which a test similar to the one analyzed in this paper was discussed, AE frequency variation was proposed as a parameter to evaluate the damage process. The results obtained in the numerical simulations of both tests are given in Figures 20 and 21.

Some remarks on the results are shown above in Figures 20 and 21:

- (i) The frequency spectrums of the AE events that occur during the damage processes in both tests are shown in Figures 20(a) and 21(a). As regards the uniaxial compression test, the energy spectrum is close to 70 kHz at the beginning of the test, while it shifts to 120 kHz at the end of the process (see Figure 20(a)). Moreover, signal energy distribution is broader in the final stage of the damage process. The same tendency was observed in Schiavi et al. (2011). In the three-point bending test, the shape of the spectrum does not show a clear tendency to change during the damage process (see Figure 21(a)).
- (ii) The highest peak frequencies (see (VII) in Figures 20(a) and 21(a)) are correlated with the discretization level. Remembering that L stands for the elemental cube side, E is Young's modulus and ρ material density, it is possible to compute the p -wave velocity in each bar as $c_\rho = (E/\rho)^{0.5}$. On the other hand, the natural vibration frequency of vibration of the normal bars of the lattice model is $f_c = 1/T_c$, where $T_c = 2 \times L/c_\rho$. By substituting the parameters corresponding to both examples, we obtain: for the uniaxial compression test $f_c = 160$ kHz, and for

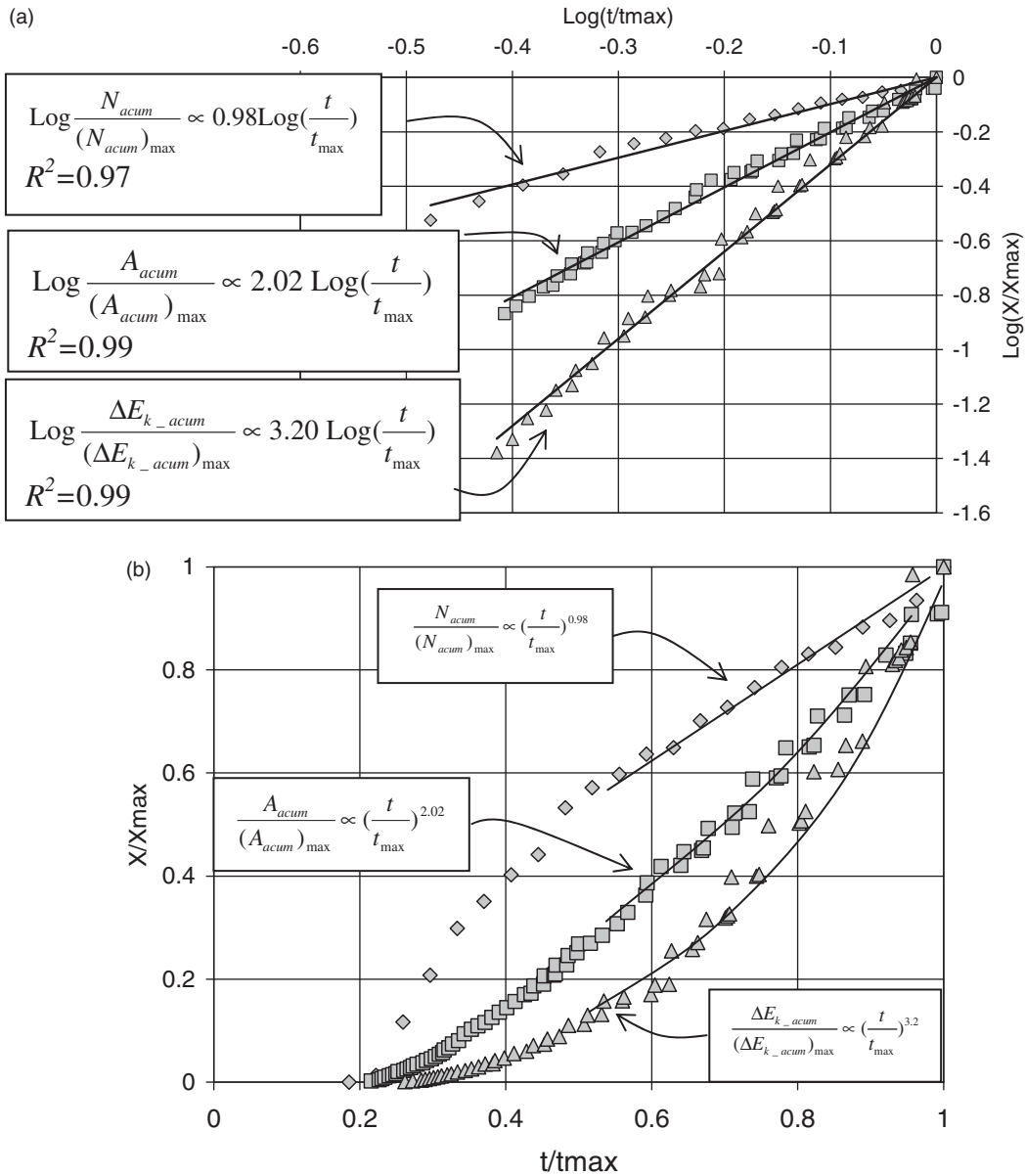


Figure 18. $N_{\text{acum}}/(N_{\text{acum}})_{\text{max}}$, $A_{\text{acum}}/(A_{\text{acum}})_{\text{max}}$ and $(E_{k_acum})/(E_{k_acum})_{\text{max}}$ vs. t/t_{max} diagrams obtained from the compression test. (a) Bi-logarithm scale. (b) Linear scale. The R value measures the linear correlation of these adjustments.

the three-point bending test $f_c = 374$ kHz. Peaks around these frequencies appear in Figures 20 and 21 and are marked with a label (VII).

- (iii) The evolution during the damage process of the two lower peak frequencies, f_1 and f_2 , and the maximum peak frequency, f_p , is shown for both examples in Figures 20(b) and 21(b). Time and frequency values are normalized to facilitate the comparison. The f_1 , f_2 and f_p frequencies are

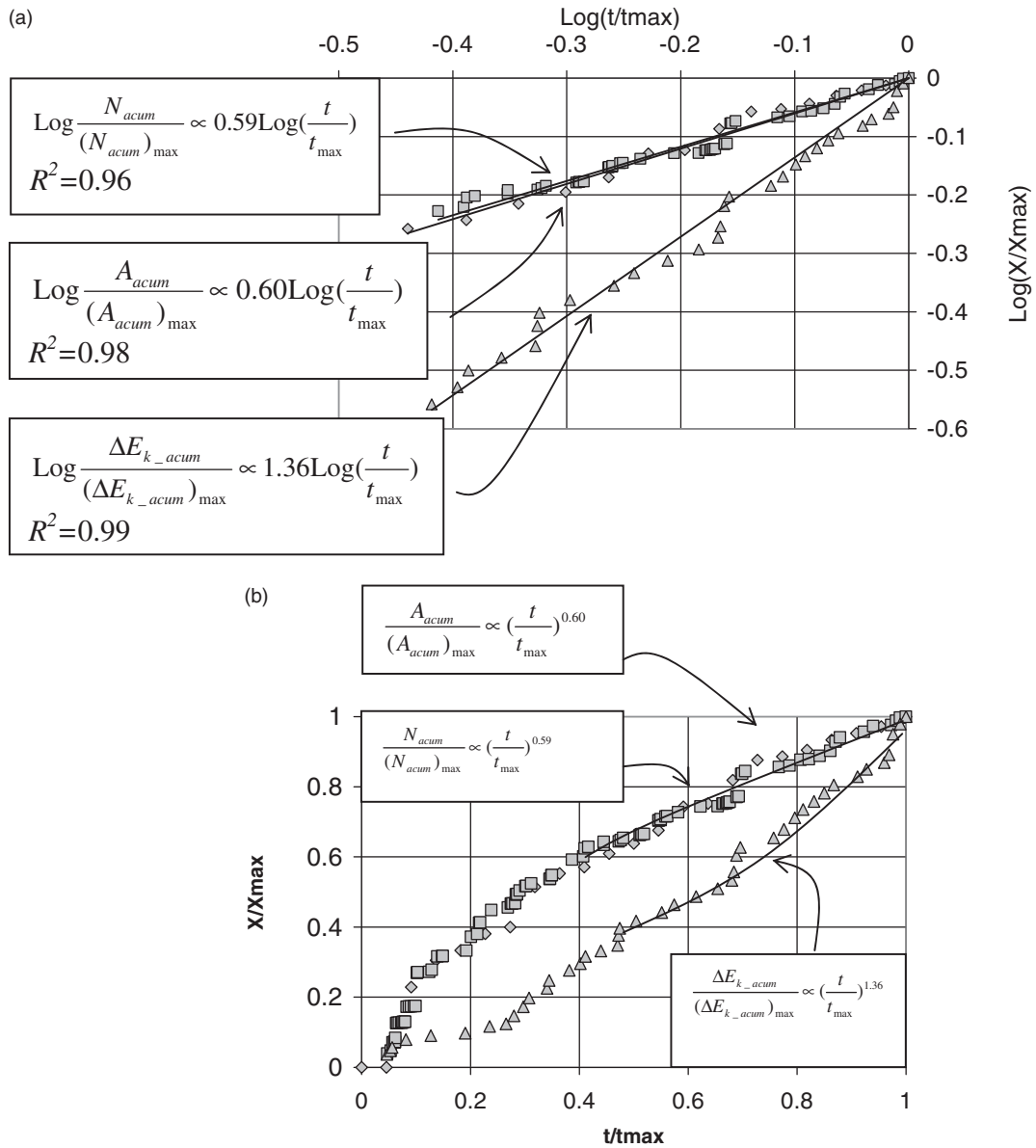


Figure 19. $N_{\text{acum}}/(N_{\text{acum}})_{\text{max}}$, $A_{\text{acum}}/(A_{\text{acum}})_{\text{max}}$ and $(E_{k_acum})/(E_{k_acum})_{\text{max}}$ vs. t/t_{max} diagrams obtained from the bending test. (a) Bi-logarithm scale. (b) Linear scale.

Table 4. β coefficients for the two specimens analyzed.

	β_N	β_A	β_K
Compr. test	0.98	2.02	3.2
Bending test	0.59	0.6	1.36

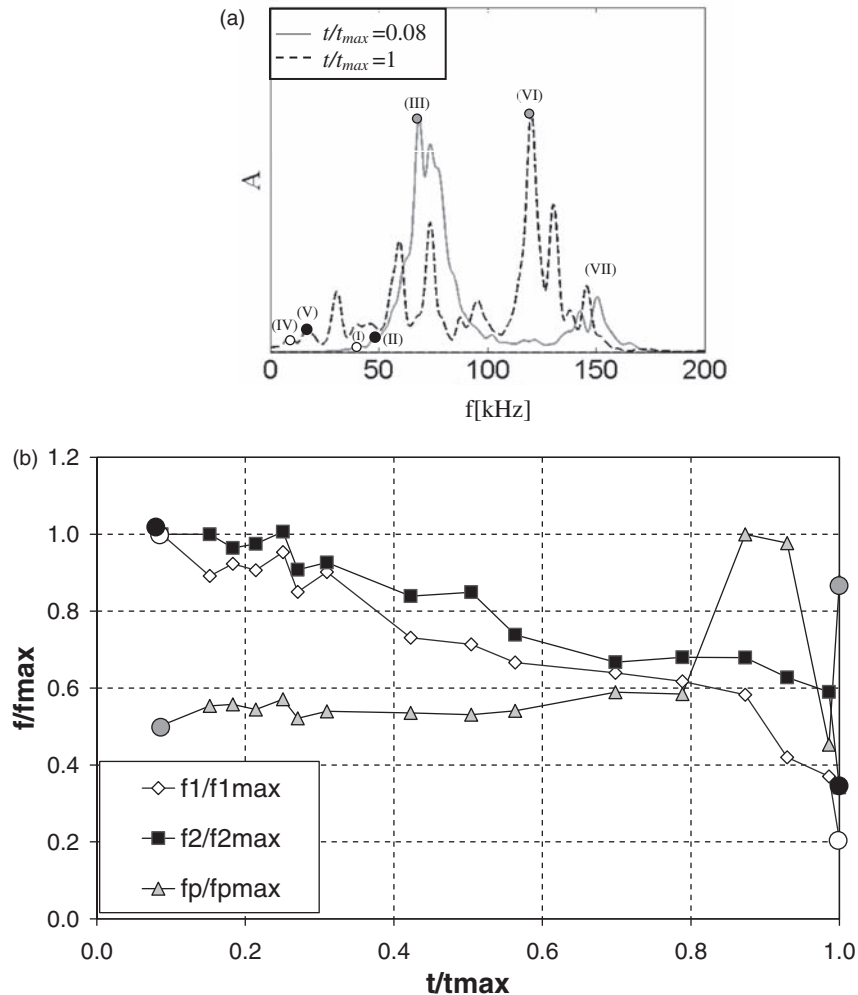


Figure 20. Frequency variations during the damage process in the compression test. (a) Two frequency spectrums were computed, at the beginning and at the end of the damage process. (b) Variations of the first (f_1), second (f_2) and maximum peak (f_p) frequencies during the damage process (in each case time and frequencies were normalized to the maximum value).

also marked with small circles in the spectrums shown in Figures 20(a) and 21(a), and marked with labels (I) to (VI). In the uniaxial compression test, Figures 20 and 21(b) show a clear tendency of the f_1 and f_2 peak frequencies to decrease with increasing damage growth. The same tendency was also observed by Schiavi et al. (2011). The values of the highest frequencies f_p does not change significantly during the damage process. Only at the final collapse their values change abruptly. Moreover, in the case of the three-point bending test, the peak frequencies, f_1 , f_2 and f_p , do not show a clear tendency to decrease during the damage process (see Figure 20(b)).

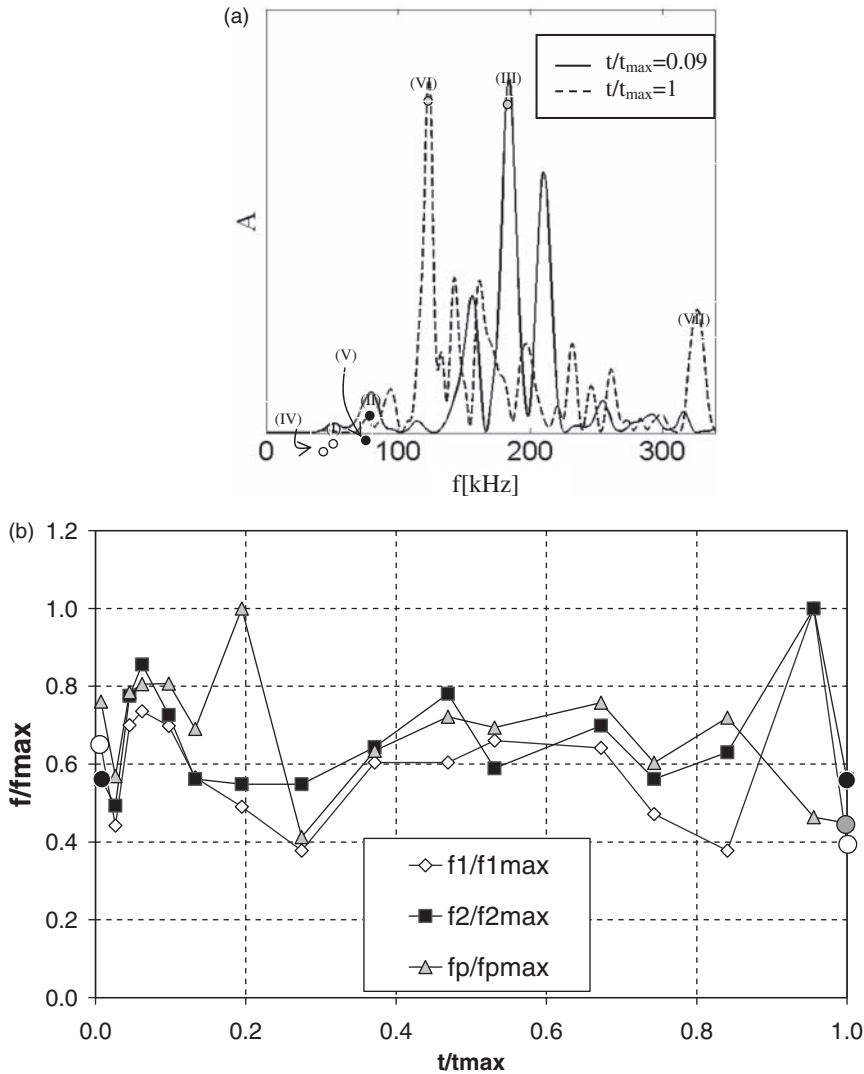


Figure 21. Frequency variations during the damage process in the three-point bending test. (a) Two frequency spectrums were computed, at the beginning and at the end of the damage process. (b) Variations of the first (f_1), second (f_2) and maximum peak (f_p) frequencies during the damage process (in each case time and frequencies were normalized to the maximum value).

Finally, the AE events vs. time diagrams obtained experimentally and numerically in the three-point bending test are shown in Figure 22. Notice that the time duration of the AE events is similar. In Figure 23, the AE events spectrums are compared and it can be seen that the numerical results present a wider spectrum. The maximum peak frequencies of the signals obtained experimentally and numerically do not match. However, for other AE events, the maximum peak values obtained numerically were in close agreement with the experimental ones.

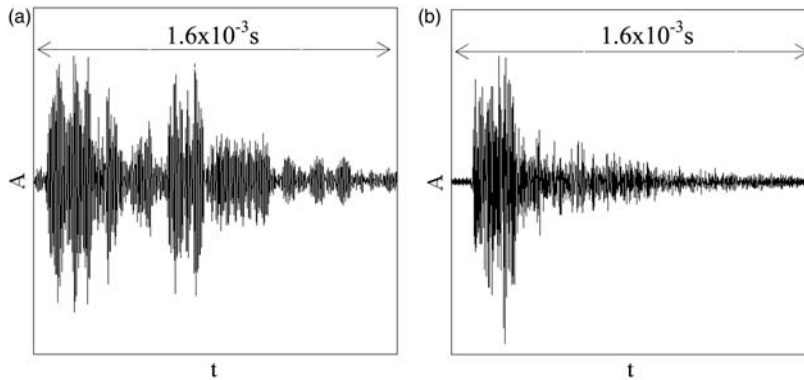


Figure 22. Typical AE signal vs. time diagrams. (a) Experimental signal. (b) Numerical signal from the three-point bending test example.

AE: acoustic emission.

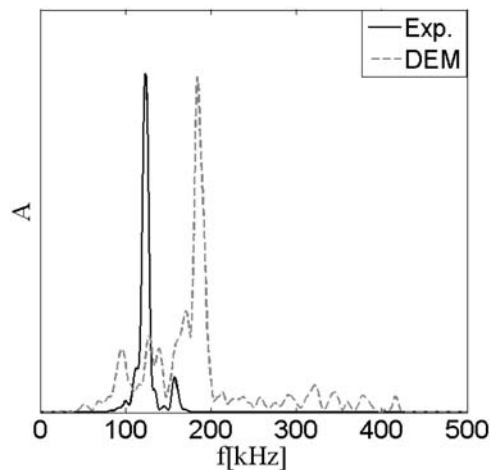


Figure 23. Comparison between the experimental and numerical spectrums obtained in the three-point bending test for a typical AE event.

AE: acoustic emission.

Conclusions

In this work, two experimental tests carried out on concrete specimens loaded up to failure are analyzed. One was a prismatic specimen subjected to uniaxial compressive loading, the other was a pre-cracked beam subjected to the three-point bending test. For both examples, experimental and numerical results are presented. The numerical simulations were performed using a version of the truss-like DEM. During the tests, the AE technique was used to monitor the damage process taking place in the specimens. The numerical and experimental results obtained in the two examples are compared, and their intrinsic differences are identified.

From these analyses, the following conclusions may be drawn.

- The comparison between the experimental and numerical results shows reasonable correlations, for both examples, in terms of conventional results, such as load vs. time and final configurations.
- In terms of the distribution of AE event amplitudes in time, the results were seen to be consistent, and any differences observed between the experimental and numerical results were accounted for. It is important to point out that the numerical b -values obtained are compatible with the experimental values and in good agreement with damage theories (Carpinteri et al., 2009b), showing a tendency to decrease during the damage process.
- The low number of AE events analyzed in the numerical simulations (fewer than 200 events in both cases) compared with the number determined by AE monitoring is an issue to be discussed in detail in relation to the results obtained. However, the aim of these numerical simulations, as mentioned above, was to identify the general trends on a preliminary base. To increase the number of AE events analyzed in the numerical simulations you need a finer discretization, something we shall do after this initial exploration of the applicability of DEM simulations to this kind of process.
- Using the AE data calculated by the numerical models, the results in terms of released energy are very useful to gain a better understanding of damage evolution of each example analyzed. The correlations between the b -values and the analogous d -values, which describe the scaling of released energy in terms of ΔE_k increments, are shown according to the fundamental law proposed by Richter (1958). On the basis of this evaluation, the numerical d -values, as well as the b -values, appear sensitive to the evolution of damage: they decrease with increasing damage and crack localization.
- The variations in time of the cumulated AE events number, AE amplitudes and cumulated increments in kinetic energy were computed, by means of the β coefficients, using the numerical models of both examples. The β coefficients made it possible to compare damage evolution in each example, showing that they are precursors of the final modalities of structural collapse.
- The numerical results obtained for the AE signal frequencies in the uniaxial compression test show variations that are consistent with the experimental data obtained by Schiavi et al. (2011). In the three-point bending test, no substantial changes in AE peak frequencies were observed instead. For this reason, it may be concluded that the clear tendency exhibited by peak frequencies to decrease during the damage process indicates that a catastrophic collapse is taking place in the specimen subjected to uniaxial compression.
- This study has shown the potential applications of the truss-like DEM not only to simulate AE monitoring analysis but also to provide a better understanding of the relationships between the basic AE parameters.
- Finally, in the application of the AE technique and the numerical approach here presented, special attention will be taken in future research to study the damage evolution in fiber-reinforced quasi-brittle materials. Three new references by Tarantino (2013) and by Nobili et al. (2012, 2013) will be taken into account for this approach: the first one about the aspects related to damage and the remaining ones with regard to the applications of the AE technique to fiber-reinforced concrete.

Acknowledgements

The financial support provided by the Regione Piemonte (Italy) through the RE-FRESCOS Project is gratefully acknowledged. The authors also thank the Brazilian agency CNPq – National Council for Scientific and Technological Development for funding this research.

References

- Aki K (1967) Scaling law of seismic spectrum. *Journal of Geophysical Research* 72: 1217–1231.
- Aki K and Richards PG (2002) *Quantitative Seismology*, 2nd ed. University Sciences Books.
- Brara A, Camborde F, Klepaczko JR, et al. (2001) Experimental and numerical study of concrete at high strain rates in tension. *Mechanics of Material* 33: 33–45.
- Carpinteri A (1994) Scaling laws and renormalization groups for strength and toughness of disordered materials. *International Journal of Solids and Structures* 31: 291–302.
- Carpinteri A, Lacidogna G and Pugno N (2007) Structural damage diagnosis and life-time assessment by acoustic emission monitoring. *Engineering Fracture Mechanics* 74: 273–289.
- Carpinteri A, Lacidogna G and Niccolini G (2006) Critical behaviour in concrete structures and damage localization by acoustic emission. *Key Engineering Materials* 312: 305–310.
- Carpinteri A, Lacidogna G, Niccolini G, et al. (2008) Critical defect size distributions in concrete structures detected by the acoustic emission technique. *Meccanica* 43: 349–363.
- Carpinteri A, Lacidogna G and Niccolini G (2009a) Fractal analysis of damage detected in concrete structural elements under loading. *Chaos, Solitons and Fractals* 42: 2047–2056.
- Carpinteri A, Lacidogna G and Puzzi S (2009b) From criticality to final collapse: evolution of the b -value from 1.5 to 1.0. *Chaos, Solitons and Fractals* 41: 843–853.
- Carpinteri A, Lacidogna G, Niccolini G, et al. (2009c) Morphological fractal dimension versus power-law exponent in the scaling of damaged media. *International Journal of Damage Mechanics* 18: 259–282.
- Chakrabarti BK and Benguigui LG (1958) *Statistical physics of fracture and breakdown in disordered systems*. Oxford: Clarendon Press.
- Chiaia B, Vervuurt A and Van Mier JG (1997) Lattice model evaluation of progressive failure in disordered particle composites. *Engineering Fracture Mechanics* 57/2/3: 301–318.
- Colombo S, Main IG and Forde MC (2003) Assessing damage of reinforced concrete beam using “ b -value” analysis of acoustic emission signals. *Journal of Materials in Civil Engineering* 15: 280–286.
- Cundall PA and Hart RD (1989) Numerical modelling of discontinua. In: Proc 1st US Conference Discrete Element Method, Golden, CO, 1–17.
- Dalguer LA, Irikura K and Riera JD (2003) Simulation of tensile crack generation by three-dimensional dynamic shear rupture propagation during an earthquake. *Journal of Geophysical Research* 108(B3): 2144.
- Dalguer LA, Irikura K, Riera JD, et al. (2001) The importance of the dynamic source effects on strong ground motion during the 1999 Chi-Chi, Taiwan, earthquake: Brief interpretation of the damage distribution on buildings. *Bulletin of the Seismological Society of America* 91: 1112–1127.
- Hillerborg A (1971) A model for fracture analysis. *Cod LUTVDG/TVBM* 300: 51–81.
- Iturrioz I, Miguel LFF and Riera JD (2009) Dynamic fracture analysis of concrete or rock plates by means of the Discrete Element Method. *Latin American Journal of Solids and Structures* 6: 229–245.
- Kanamori H and Anderson DL (1975) Theoretical basis of some empirical relations in seismology. *Bulletin of the Seismological Society of America* 5: 1073–1095.
- Kosteski L, Barrios R and Iturrioz I (2008) Determinación de Parámetros Fractomecánicos Estáticos y Dinámicos utilizando el Método de los Elementos Discretos compuestos por barras. *Revista Internacional Métodos Numéricos para Cálculo y Diseño en Ingeniería*. *Cimne* 24: 323–343.
- Kosteski L, Barrios R and Iturrioz I (2009) Fractomechanics parameter calculus using the Discrete Element Method. *Latin American Journal of Solids and Structures* 6: 301–321.
- Kosteski LE, Barrios R and Iturrioz I (2012) Crack propagation in elastic solids using the truss-like discrete element method. *International Journal of Fracture* 174: 139–161.
- Kosteski L, Iturrioz I, Batista RG, et al. (2011) The truss-like discrete element method in fracture and damage mechanics. *Engineering Computations* 6: 765–787.
- Krajcinovic D (1996) *Damage Mechanics*. Elsevier, Amsterdam.
- Kurz JH, Finck F, Grosse CU, et al. (2006) Stress drop and stress redistribution in concrete quantified over time by the b -value analysis. *Structural Health Monitoring* 5: 69–81.
- Lemaitre J and Chaboche JL (1990) *Mechanics of Solid Materials*. Cambridge: University Press.

- Lu C, Mai YW and Xie H (2005) A sudden drop of fractal dimension: a likely precursor of catastrophic failure in disordered media. *Philosophical Magazine Letters* 85: 33–40.
- Mastilovic S (2011a) Some observations regarding stochasticity of dynamic response of 2D disordered brittle lattices. *International Journal of Damage Mechanics* 20: 245–265.
- Mastilovic S (2011b) Further remarks on stochastic damage evolution of brittle solids under dynamic tensile loading. *International Journal of Damage Mechanics* 20: 900–992.
- Miguel LFF, Riera JD and Iturrioz I (2008) Influence of size on the constitutive equations of concrete or rock dowels. *International Journal for Numerical and Analytical Methods in Geomechanics* 32: 1857–1188.
- Miguel LFF, Iturrioz I and Riera JD (2010) Size effects and mesh independence in dynamic fracture analysis of brittle materials. *Computer Methods Modeling in Engineering & Sciences* 56: 1–16.
- Munjiza A (2009) Special issue on the discrete element method: aspects of recent developments in computational mechanics of discontinua. *Engineering Computations* 26: 6.
- Munjiza A, Bangash T and John NWM (2004) The combined finite-discrete element method for structural failure and collapse. *Engineering Fracture Mechanics* 71: 469–483.
- Nayfeh AH and Hefzy MS (1978) Continuum modeling of three-dimensional truss-like space structures. *AIAA Journal* 8: 779–787.
- Nobili A, Lanzoni L and Tarantino AM (2012) Performance evaluation of a polypropylene-based draw-wired fibre for concrete structures. *Construction and Building Materials* 28: 798–806.
- Nobili A, Lanzoni L and Tarantino AM (2013) Experimental investigation and monitoring of a Polypropylene-based fiber reinforced concrete road pavement. *Construction and Building Materials* 38: 491–496.
- Ohtsu M (1996) The history and development of acoustic emission in concrete engineering. *Magazine of Concrete Research* 48: 321–330.
- Pollock AA (1973) Acoustic emission-2: acoustic emission amplitudes. *Non-Destruct Test* 6: 264–269.
- Rabczuk T and Belytschko T (2004) Cracking particles: a simplified meshfree method for arbitrary evolving cracks. *International Journal for Numerical Methods in Engineering* 61(13): 2316–2343.
- Rabczuk T and Belytschko T (2007) A three-dimensional large deformation meshfree method for arbitrary evolving cracks. *Computer Methods in Applied Mechanics and Engineering* 196(29–30): 2777–2799.
- Rabczuk T, Bordas S and Zi G (2007) A three-dimensional meshfree method for continuous multiple crack initiation, nucleation and propagation in statics and dynamics. *Computational Mechanics* 40(3): 473–495.
- Rao MVMS and Lakshmi KJP (2005) Analysis of b -value and improved b -value of acoustic emissions accompanying rock fracture. *Current Science* 89: 1577–1582.
- Richter CF (1958) *Elementary Seismology*. San Francisco and London: W. H. Freeman.
- Riera JD (1984) Local effects in impact problems on concrete structures. In: *Proceedings, conference on structural analysis and design of nuclear power plants*, Porto Alegre, RS, Brazil, Vol. 3, CDU 264.04:621.311.2:621.039.
- Riera JD and Iturrioz I (1995) Discrete element dynamic response of elastoplastic shells subjected to impulsive loading. *Communications in Numerical Methods in Engineering* 11: 417–426.
- Riera JD and Iturrioz I (1998) Discrete element model for evaluating impact and impulsive response of reinforced concrete plates and shells subjected to impulsive loading. *Nuclear Engineering and Design* 179: 135–144.
- Rinaldi A and Lai YC (2007) Statistical damage theory of 2D lattices: Energetics and physical foundations of damage parameter. *International Journal of Plasticity* 23: 1769–1825.
- Rinaldi A, Krajcinovic D, Peralta P, et al. (2008) Lattice models of polycrystalline microstructures: A quantitative approach. *Mechanics of Materials* 40: 17–36.
- Rios RD and Riera JD (2004) Size effects in the analysis of reinforced concrete structures. *Engineering Structures* 26: 1115–1125.
- Rundle J, Turcotte D, Shcherbakov R, et al. (2003) Statistical physics approach to understanding the multiscale dynamics of earthquake fault systems. *Reviews of Geophysics* 4: 8755–81209.
- Schiavi A, Nicolini G, Tarizzo P, et al. (2011) Acoustic emissions at high and low frequencies during compression tests in brittle materials. *Strain* 47(Suppl 2): 105–110.

- Schnaid F, Spinelli L, Iturrioz I, et al. (2004) Fracture mechanics in ground improvement design. *Ground Improvement* 8: 7–15.
- Scholz CH (1968) The frequency-magnitude relation of microfracturing in rock and its relation to earthquakes. *Bulletin of the Seismological Society of America* 58: 99–415.
- Scholz CH (2002) *The Mechanics of Earthquakes and Faulting*, 2nd ed. New York, US: Cambridge University Press.
- Shiotani T, Fujii K, Aoki T, et al. (1994) Evaluation of progressive failure using AE sources and improved *b*-value on slope model tests. *Progress in Acoustic Emission* 7: 529–534.
- Tarantino AM (2013) Equilibrium paths of a hyperelastic body under progressive damage. *Journal of Elasticity*. DOI: 10.1007/s10659-013-9439-0.
- Turcotte DL, Newman WI and Shcherbakov R (2003) Micro and macroscopic models of rock fracture. *Geophysical Journal International* 152: 718–728.